Pergamon

Int. J. Heat Mass Transfer. Vol. 40, No. 9, pp. 2173–2185, 1997

0017–9310/97 $17.00+0.00

PII: S0017–9310(96)00246–3

Natural convection heat transfer in vertical channels with and without transverse square ribs

GIOVANNI TANDA

Dipartimento di Termoenergetica e Condizionamento Ambientale, Università di Genova, via all'Opera Pia 15/a, I-16145 Genova, Italy

(*Received* 3 *May* 1996 *and in final form* 26 *June* 1996)

Abstract—Experiments were performed to determine heat transfer data for the natural convective flow of air in vertical channels with one surface roughened by transverse square ribs and the opposite surface smooth. Uniform wall temperature conditions were imposed on the ribbed side, while the smooth side remained unheated. Additional experiments were carried out in vertical channels without ribs, under the same channel geometry and thermal conditions. A schlieren optical technique was used to reconstruct the thermal field and to obtain distributions of heat transfer coefficients. The presence of ribs was found to alter heat transfer considerably, causing thermally inactive regions just upstream and downstream of each protrusion. Consequently, the heat transfer performance of the ribbed channel turned out to be lower than that of the corresponding smooth channel.

INTRODUCTION

Natural convection in vertical channels is encountered in a number of technological applications. This has motivated a large body of experimental and analytical studies of this topic. Bar-Cohen and Rohsenow [1] have correlated most of the existing data by using composite relationships giving heat transfer coefficients and other useful quantities (such as the optimum channel spacing to maximise heat transfer) for natural convection in heated vertical channels. If large-scale roughness elements are present on one or both surfaces forming the vertical channel, the natural convection flow may significantly alter. There are two substantial reasons for investigating natural convection heat transfer in rough channels. Establishing whether the protrusions yield heat transfer enhancements is of great importance in applications where the maximisation of the heat transfer rate is the prime consideration. Moreover, there are situations (surfaces of buildings, electronic circuit boards) in which the roughness occurs naturally and is not added for the specific purpose of modifying heat transfer performance. Understanding the thermal behaviour of these systems is essential for their correct design.

Roughness elements may significantly affect the free convection heat transfer in vertical channels owing to the following circumstances: (i) the blockage effect associated with the presence of protrusions could provoke a weaker induced flow, potentially reducing the heat transfer; (ii) the roughness could induce disturbances in the overlying laminar boundary layer, thus causing premature transition to turbulence; (iii) the roughness elements, if heated, add an extra heat transfer surface area.

Compared with the abundant literature on natural convection in channels with smooth surfaces, relatively few and recent studies have dealt with the effect of large-scale roughness elements on free convection heat transfer in channels. The influence of a single two-dimensional obstruction in vertical channels has been investigated by Hung and Shiau [2], and Said and Krane [3]. Natural convection from arrays of protrusions on a vertical surface has been experimentally studied by Joshi *et al.* [4] and Bhavnani and Bergles [5]. More recently, the effect of heated protrusions in vertical channels has been studied by Kelkar and Choudhury [6] and by Acharya and Mehrotra [7]. Direct comparisons with the smooth channel/smooth surface performance under the same geometric and thermal conditions are presented in ref. [3] (geometry: a single rounded protrusion in a vertical channel; thermal condition: Uniform Wall Temperature or Uniform Heat Flux on both sides), in ref. [5] (several rectangular ribs on a vertical smooth surface, UWT) and in ref. [7] (several square ribs on both sides of a vertical channel, UWT or UHF on both sides). These studies reveal that a significant influence on natural convection flows is exerted by single/multiple obstructions. Owing to the numerous geometric parameters involved and the different thermal boundary conditions, further investigations are required in order to quantitatively define heat transfer characteristics for ribbed channels.

The present work is aimed at making a contribution to this area of research: information on local and

NOMENCLATURE

A	heat transfer surface area
c_p	specific heat at constant pressure of the fluid
e	square rib height
g	acceleration of gravity
H	channel height
h	heat transfer coefficient
k	thermal conductivity of the fluid
L	plate length
Nu	Nusselt number, equations (6) and (10)
Nu^*	channel Nusselt number, equation (12)
n_r	number of repeated ribs
P	rib pitch
Q	convective heat transfer rate
Ra	Rayleigh number, equation (5)
Ra^*	channel Rayleigh number, equation (11)
S	channel spacing
T	absolute temperature
t	plate thickness
x, y, z	spatial coordinates
x'	coordinate along the ribbed plate surface.

Greek symbols

α	angular deflection of the light ray
β	coefficient of thermal expansion of the fluid
Δ	deviation of the light ray
μ	dynamic viscosity of the fluid
ρ	density of the fluid
ϑ	dimensionless temperature
Ω	constant in equations (1), (2) and (4).

Subscripts

av	average (energy balance)
o	obtained from integration of optical data
r	referring to the ribbed plate
s	referring to the smooth plate
w	wall conditions
y	referring to y-direction
∞	ambient (or channel inlet) conditions.

average heat transfer coefficients and the thermal field are provided for vertical channels formed by a rib-roughened heated plate (UWT condition) and an opposing smooth unheated plate. The work was conducted experimentally using the schlieren optical technique; the heat transfer mechanism was natural convection in air. For the purpose of comparison, experiments for smooth vertical channels in similar geometric and thermal conditions were also performed.

EXPERIMENTAL APPARATUS AND PROCEDURE

The test section consisted of a plate (termed "heated plate"), made up of two aluminum sheets and three plane electrical resistances sandwiched in between, and two shrouding vertical walls. The plate was vertically suspended and heated by supplying a given amount of power to the resistances. The shrouding walls were smooth, unheated and placed in order to form two adjacent, symmetrical, vertical channels, as shown in Fig. 1. Two different aluminum plates have been considered in this study: with smooth surfaces (Fig. 1a) or with transverse, square-cross-sectioned ribs on both sides (Fig. 1b). The ribs were made integral with the baseplate to guarantee the absence of contact resistance. Owing to the high cost of producing the ribbed plate, the geometric parameters of the square ribs (height and pitch) were kept constant in this study. Aluminum was chosen for its high thermal conductivity, low thermal emittance, and easy machinability.

The dimensions of the heated plate were: overall thickness (without ribs) $t = 12$ mm, height $H = 175$ mm, length $L = 300$ mm. The length was set much greater than the other dimensions in order to favour a two-dimensional thermal field in the channels. The square ribs, when present, had a height (e) of 4.85 mm and were regularly spaced at intervals of 35 mm, resulting in a pitch-to-height ratio P/e of 7.2. In such a way, five ribs for each side of the heated plate were considered ($n_r = 5$). The unheated shrouding walls, having the same height and length as the heated plate, were made up of 3 mm-thick sheets of perspex, covered by a reflective plastic film on the sides facing the aluminum plate (to reduce radiant exchange) and

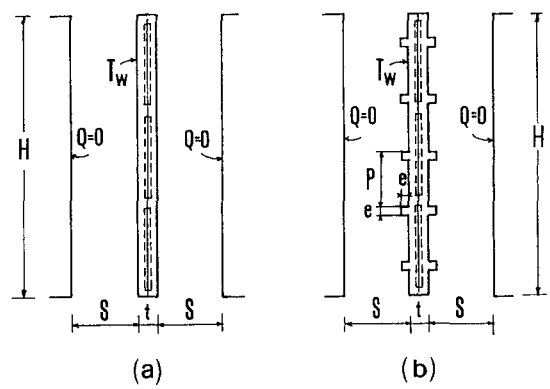

Fig. 1. Schematic layout of the vertical channel configurations; (a) a smooth heated plate shrouded by unheated walls, (b) a rib-roughened heated plate shrouded by unheated walls.

insulated by a 20 mm layer of polystyrene on the outer surfaces (to minimise heat conduction through the side walls). The spacing S between each unheated wall and the heated plate, set equal on both sides, was varied between 8.75 mm and 70 mm, in order to cover a range of the channel aspect ratio S/H from 0.05 to 0.4.

Both the plate and the surroundings were instrumented with fine-gauge, chromel-alumel thermocouples, calibrated to ± 0.1 K. Numerous thermocouples were embedded in the wall of the heated plate at different locations through 0.5-mm-dia holes drilled into the rear surfaces of the two coupled aluminum sheets. Care was taken to drill the holes as close to the exposed surfaces as possible. For the ribbed plate, temperature was monitored both at the rib edges and in the inter-rib region. The ambient air temperature was measured by five shielded thermocouples situated just below the plate array. Additional thermocouples were used to detect surface temperature on the unheated side walls. Details of the housing of thermocouples (for the ribbed plate configuration) are shown in Fig. 2.

The power input supplied to the aluminum plate was transferred to the surroundings by natural convection and radiation. Since the thermal resistance of the plate material was very low, owing to the high thermal conductivity of aluminum, the plate was expected to be virtually isothermal. This condition was achieved by simply connecting the three plane resistances in series, albeit to three independent power supplies. The degree of uniformity of the surface temperature was checked by comparing the independent readings obtained in different spots (including the vertical symmetry line of the plate as well as lateral edges). For all the experimental runs, the temperature readings were uniform within $\pm 2\%$ of the mean plate-to-ambient temperature difference.

As previously noted, all of the heating power supplied to the plate was dissipated at its exposed surfaces

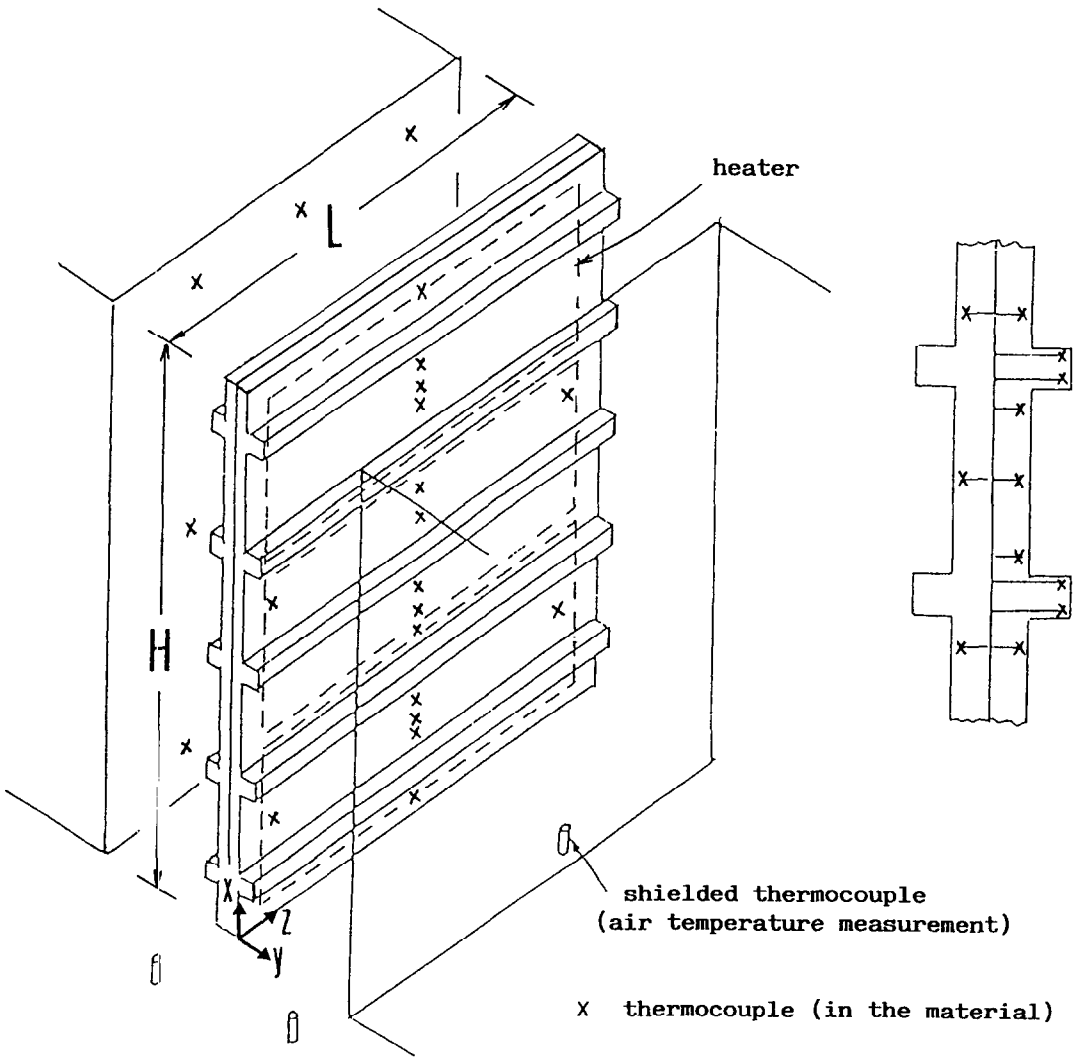

Fig. 2. Detail of the housing of the thermocouples (X) in the plate and surroundings (ribbed plate configuration).

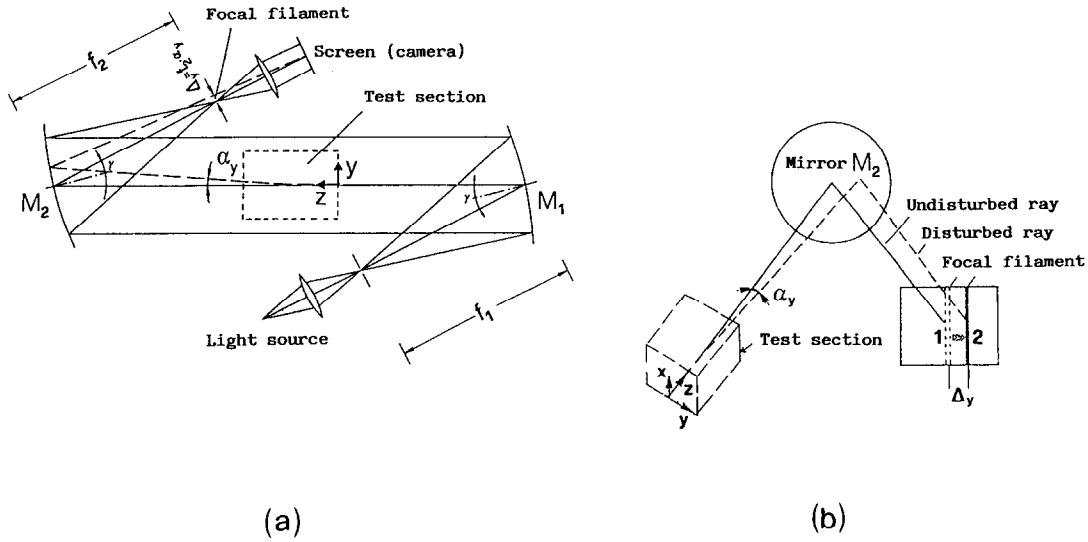

Fig. 3. (a) Schlieren apparatus (top view): M_1 and M_2 are 0.38-m-diameter concave mirrors (with focal lengths f_1 and f_2, respectively), α_y is the angular deflection of the light ray (in the y–z plane) and Δ_y is the corresponding light deviation at the focal plane of mirror M_2 ($f_1 = f_2 = 1.9$ m, $\gamma = 9°$, distance between mirrors about 8 m); (b) measurement of light deviation Δ_y at the focal plane of mirror M_2: the focal filament is shifted from position 1 to position 2.

by natural convection and radiation. The radiation heat transfer was expected to be small because of the low thermal emittance of aluminum surfaces, which was measured by a radiometric apparatus as 0.12 ± 0.02 in the temperature range of interest. The two vertical channels formed by the heated plate and the shrouding walls were confined on four sides by glass walls with open grids at the bottom. Runs conducted without the glass walls revealed negligible effects on heat transfer performance, but the walls were deemed necessary to minimize extraneous air-current effects that might disturb the optical measurements.

A schlieren optical system was used to reconstruct the thermal field and to perform measurements of local heat transfer coefficients. The schlieren system is schematically shown in Fig. 3a. A non-coherent light beam from a vertical slit source, collimated by the concave mirror M_1, passes through the test section. A second concave mirror M_2 is then used to project a real image of the slit source in the focal plane and a real image of the test section onto a screen or camera. Owing to the inhomogeneities of the fluid refractive index around the heated plate, the light rays undergo angular deflections. Regions of the optical field characterised by the same light deflection α_y in the y–z plane can be identified by shifting an opaque vertical filament in the focal plane of mirror M_2, as shown in Fig. 3b. When a disturbed light ray is stopped by the focal filament, the image of the corresponding region of fluid will appear dark on the screen, while the remaining field will be bright. The deflection α_y of a disturbed ray can be recorded by measuring, in the focal plane of mirror M_2, the distance Δ_y between the middle of the undisturbed image of the slit source and the centreline of the filament, i.e. the distance between the filament positions 1 and 2 displayed in Fig. 3b. It can be easily shown that the distance Δ_y (corresponding to the ray shift at the focal plane of mirror M_2) is given by $f_2 \cdot \alpha_y$, f_2 being the focal length of the mirror M_2. If the thermal field is assumed to be two-dimensional (i.e. temperature is independent of z-coordinate) the shift Δ_y of each light ray can be related to the local temperature gradient in the fluid by the following expression

$$\Delta_y = \Omega \cdot (\partial T/\partial y)/T^2 \qquad (1)$$

where $T = T(x, y)$ is the fluid (absolute) temperature, y is the direction in which the light deflection is recorded and Ω is a constant depending on the fluid, the pressure, the length of the heated plate and geometric parameters of the optical components. In the present experiment, Ω was equal to -0.0456 m^{2}K. The temperature reconstruction procedure is based on a set of photographs (for each experimental run) obtained with the focal filament placed at different distances Δ_y from the undisturbed slit-source image. A typical example of a photograph taken by the schlieren apparatus (for the ribbed plate) is reported in Fig. 4. By identifying for each photograph the coordinates of the centreline of the filament shadow, it is possible to obtain the profile of lines of constant light-deviation values Δ_y and thus, taking into account equation (1), reconstruct the temperature distribution in the entire optical field.

The local heat transfer coefficient can be directly obtained from schlieren images without having to reconstruct the whole thermal field. Indeed, if the focal filament is moved until its shadow intersects (in the

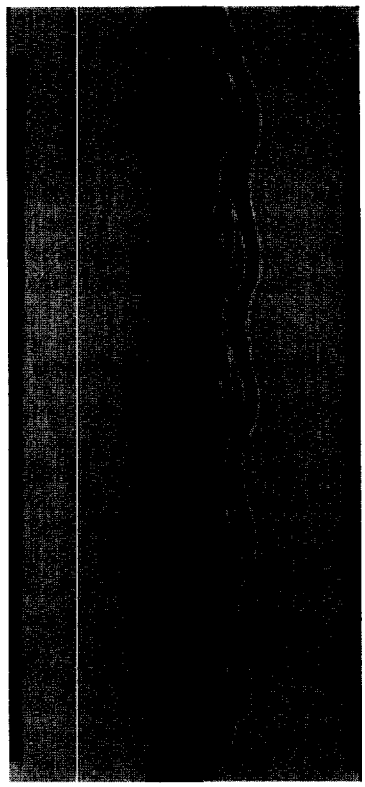

Fig. 4. Schlieren image recorded for the ribbed plate configuration ($Ra = 1.8 \cdot 10^7$, $S/H = 0.2$, $\Delta_y = 1.4$ mm).

image projected on the camera) the vertical surface profile, the displacement of the filament corresponds to the deviation Δ_w of the light ray passing in the vicinity of the wall at the desired location. The relation between light deviation Δ_w and the local heat transfer coefficient can be easily shown as follows. By applying equation (1) at the heated walls, one obtains

$$\Delta_w = \Omega \cdot (\partial T/\partial n)_w / T_w^2 \tag{2}$$

where $(\partial T/\partial n)_w$ is the fluid temperature gradient, in the direction n normal to the plate surface, evaluated at the wall, and T_w is the wall temperature. By introducing the local heat transfer coefficient, defined as

$$h = \frac{-k_w(\partial T/\partial n)_w}{(T_w - T_\infty)} \tag{3}$$

where k_w is the thermal conductivity of the fluid at the wall temperature and T_∞ is the ambient (or inlet) air temperature, it follows that

$$h = -k_w \Delta_w T_w^2 / (\Omega(T_w - T_\infty)) \tag{4}$$

Since both the slit source and the focal filament are able to rotate through a 90° angle on the focal planes of mirror M_1 and M_2 respectively, the lines at constant light-deflection values can be detected on the y–z plane as well as on the x–z plane. In the same way, equation (4) can be used to evaluate heat transfer coefficients along the vertical surfaces, by recording light deviations at the wall along the y-direction, as well as along the horizontal surfaces, such as on the top and bottom sides of ribs, by recording light deflection at the wall along the x-direction. Further details of the derivation of fundamental schlieren formulae as well as of the thermal field reconstruction procedure are given in refs. [8–10].

For both plate configurations (without and with ribs) experimental runs were performed according to the following procedure:

(i) Positioning of the unheated side walls by setting the desired value of the interplate spacing S.

(ii) Heating of the plates by a given input of electrical power into the heaters, in order to achieve the desired uniform temperature over the aluminum plates. The majority of tests were conducted by imposing a mean temperature difference between the heated plate and the ambient air of 45 K, giving a Rayleigh number Ra (based on the channel height H as characteristic length) of $1.8 \cdot 10^7$. For the ribbed plate, additional runs were conducted at wall-to-fluid temperature differences in the range 10–45 K.

(iii) In the steady state, measurements of wall and ambient air temperatures by averaging the readings from the thermocouple arrays deployed in the material and ambient air, respectively. For a number of experiments, the reconstruction of the thermal field was performed from a set of schlieren photographs taken, for each run, by moving the focal filament either in the y-direction or in the x-direction.

(iv) Optical measurement of the light deflections near the vertical walls in order to obtain the local heat transfer coefficients at several locations along the heated plate surfaces, for both vertical and horizontal boundaries.

The Rayleigh number, the Nusselt number and a convenient dimensionless temperature can be introduced as follows

$$Ra = c_p \rho^2 \beta g H^3 (T_w - T_\infty)/(k\mu) \tag{5}$$

$$Nu = hH/k \tag{6}$$

$$\vartheta = (T - T_\infty)/(T_w - T_\infty) \tag{7}$$

where k, β, μ, ρ and c_p represent the thermal conductivity, the thermal expansion coefficient, the dynamic viscosity, the density and the specific heat (at constant pressure) of the fluid, respectively, and g is the gravitational acceleration.

Two different approaches were used to evaluate the average heat transfer characteristics. From the energy balance applied to the heated plate, the net convective heat transfer rate Q exchanged with the air in the channels is based on the following equation

$$Q = Q_{el} - Q_{rad} - Q_{edge} \tag{8}$$

where Q_{el} is the measured electrical power input, Q_{rad} is the overall radiant heat transfer and Q_{edge} is the convective heat transfer from the edge surfaces of the heated plate. The area of edge surfaces

is $2\times(H+L)\times t$ without the ribs and $2\times(H+L)\times t+4\times n_r\times e^2$ in the presence of n_r repeated ribs of height e on both sides. The radiant heat transfer was determined by calculation, using a diffuse, gray-body network, with interactions between each side of the plate and the surroundings. In general, the radiant heat transfer was between 10% and 16% of the total power input. The convective heat transfer from edge surfaces was estimated by using standard relationships available in heat transfer textbooks, and accounted for 7–10% of the total power input.

The average heat transfer coefficient can be then evaluated from

$$h_{av}=Q/[A\cdot(T_w-T_\infty)] \tag{9}$$

where the surface area A is equal to $2\times H\times L$ without the ribs and to $(2\times H\times L+2\times n_r\times 2e\times L)$ in the presence of n_r repeated square ribs (of height e) on both sides.

In addition to the average heat transfer coefficient deriving from the energy balance, an average value h_o can be obtained from the numerical integration of local coefficients h measured according to equation (4). After runs, this quantity turned out to be only slightly different (within 6%) from the coefficient h_{av} obtained from the energy balance. Since the integration of optical data was based on a discrete number of local values, the heat transfer coefficient h_{av} given by the energy balance was preferred in the presentation of results for the definition of the average Nusselt number Nu_{av}:

$$Nu_{av}=h_{av}H/k \tag{10}$$

Heat transfer characteristics have also been expressed using the channel Rayleigh number and the channel Nusselt number defined as follows:

$$Ra^*=c_p\rho^2\beta g S^4(T_w-T_\infty)/(Hk\mu) \tag{11}$$

$$Nu^*=h_{av}S/k \tag{12}$$

The fluid properties appearing in the dimensionless groups previously introduced were evaluated at the reference temperature $T^*=(T_w+T_\infty)/2$.

The uncertainties of the main quantities obtained from the experimental investigation were estimated (at the 95% confidence level) according to the procedure outlined in [11]. Uncertainties in the Rayleigh number Ra and the Nusselt number Nu_{av} are mainly affected by the uncertainty in the measurements of the mean plate-to-fluid temperature difference (T_w-T_∞) for the former, and by the uncertainties in (T_w-T_∞) and the electrical power input for the latter. Since the wall temperature uniformity was good and the input power evaluation was very accurate, tolerances in Ra and Nu_{av} (or h_{av}) were reduced to a few percent (5% and 7%, respectively).

The uncertainty in local heat transfer coefficient h (or local Nusselt number Nu) is strictly related to the accuracy of the light deviation Δ_w readings. In the field of Δ_w values between 0.8 mm and 8 mm (in which the majority of measurements were performed) the uncertainty in h values was estimated to range from 20% (at the smallest light deviations) to 8% (at the largest light deviations). Since integration averages the noise in the local Nusselt number values, the average heat transfer coefficients h_o are likely to be more accurate than the local data. The uncertainty in the reconstructed temperature T was about 2–4% of the wall-to-ambient temperature difference, giving a maximum uncertainty of ± 0.04 in ϑ values.

RESULTS AND DISCUSSION

First, attention is devoted to experiments conducted with the smooth (unribbed) plate. Since heat transfer characteristics of asymmetrically heated vertical smooth channels are already available in the literature (see ref. [1], for instance), only a limited number of results are presented. Figure 5 shows the distributions of local heat transfer coefficients and Nusselt number values, evaluated by the Schlieren method, for different values of the channel aspect ratio S/H. The Rayleigh number was $Ra=1.8\cdot 10^7$, corresponding to the mean wall-to-fluid temperature difference of 45 K. For each S/H value, the local heat transfer coefficient was evaluated by an average of the values recorded, at the same elevation, on the left and right sides of the heated plate. As is evident from the figure, there are only small differences between the heat transfer coefficients obtained for S/H between 0.1 and 0.4. Entrance effects are responsible for the larger heat transfer coefficients at the leading edge as S/H is progressively reduced. For the lowest aspect ratio investigated ($S/H=0.05$), the heat transfer coefficient distribution starts from a very high value but then sharply decreases as the vertical coordinate is increased, owing to the interaction of the growing thermal boundary layer with the unheated plate.

The average heat transfer coefficients h_{av} (from energy balance) and h_o (from integration of optical data) are plotted as a function of the channel aspect ratio S/H in Fig. 6. From both the energy balance and the optical measurements the aspect ratio, for the range explored here, is found to affect the average heat transfer coefficient only slightly. A maximum value at $S/H=0.1$, mainly connected to entrance effects, is shown by both the approaches used to evaluate overall heat transfer performance.

In terms of channel Rayleigh and Nusselt numbers, experimental heat transfer results for the smooth channel can be successfully correlated (within $\pm 4\%$) by the Bar-Cohen and Rohsenow composite relationship [1]

$$Nu^*=[144/(Ra^*)^2+2.873/(Ra^*)^{0.5}]^{-0.5} \tag{13}$$

where the Ra^* range covered by experiments was 10^2–$5\cdot 10^5$.

The main purpose of this study was to establish the effect that transverse square ribs produce on the heat

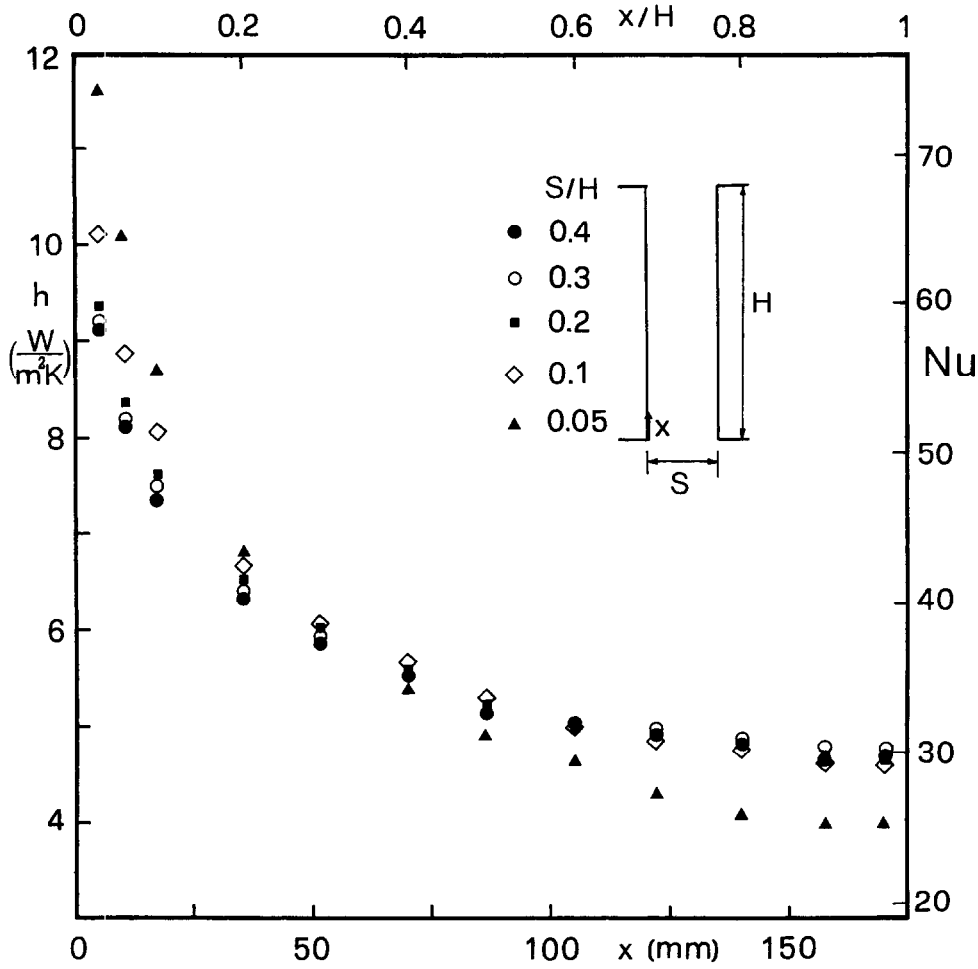

Fig. 5. Distributions of the heat transfer coefficients (and *Nu* values) for different *S*/*H* values, smooth plate configuration, $Ra = 1.8 \cdot 10^7$.

transfer characteristics of asymmetrically heated vertical channels. Therefore, the majority of experiments were conducted in the presence of the ribbed plate assembly. For this configuration, both thermal fields and local heat transfer coefficient distributions are presented. In order to reconstruct the thermal field for a given experiment, the pattern of lines at equal light deviation has to be determined from optical measurements. A typical pattern of lines at equal Δ_y is reported in Fig. 7. Taking into account the relationship between Δ_y and local temperature T (see equation (1)), the mathematical treatment of the pattern of Δ_y lines enables the isothermal lines to be identified. The isotherm contours, based on the dimensionless temperature ϑ, are presented in Fig. 8 for three values of the aspect ratio S/H and for $Ra = 1.8 \cdot 10^7$ ($T_w - T_\infty = 45$ K). The thermal fields have been extracted for the first module (space between the first and second ribs from the bottom) and for the last module (space between the fourth and fifth ribs), as shown in the sketch. In general, the isotherm contours

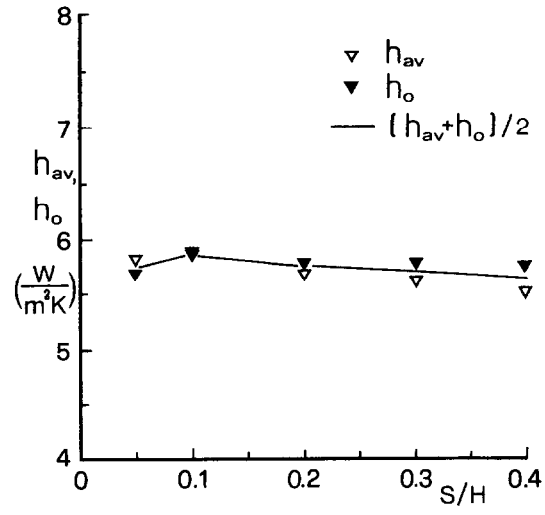

Fig. 6. Average heat transfer coefficients h_{av} (from the energy balance) and h_o (from integration of optical data), smooth plate configuration ($Ra = 1.8 \cdot 10^7$).

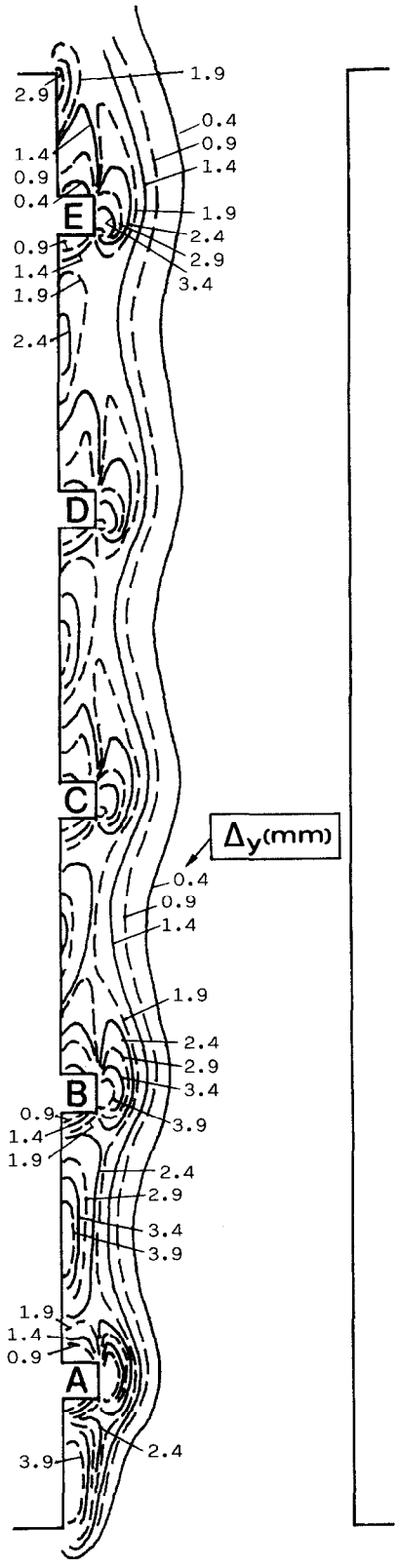

Fig. 7. Lines at equal light deviation Δ_y, ribbed plate configuration ($Ra = 1.8 \cdot 10^7$, $S/H = 0.2$).

clearly show the dead zones just upstream and downstream of each rib, as well as the wall regions of high heat transfer performance on the vertical sides of the ribs and between the ribs, where the thermal boundary layer is relatively thin. It can be seen that, in the case of a large aspect ratio ($S/H = 0.4$, Fig. 8a), the isotherms from $\vartheta = 0.1$ to 0.9 are packed close to the ribbed wall. This means that a considerable part of the fluid driven upwards through the channel remains practically unheated. As the aspect ratio is reduced, the temperature attained by air flowing into the channel progressively increases. For instance, at $S/H = 0.1$ (Fig. 8b), the buoyancy-induced air flowing through the last module possesses a dimensionless temperature exceeding 0.1 at any given point. At the lowest aspect ratio ($S/H = 0.05$, Fig. 8c), ϑ is always higher than 0.3 in the first module and reaches $\vartheta = 0.6-0.65$ at the unheated wall close to the exit of the last module.

Attention is now turned to heat transfer coefficient distributions. Figures 9–11 show, in sequence, the local heat transfer coefficients and Nusselt number values along the wall profile, again for $S/H = 0.4$ (Fig. 9), 0.1 (Fig. 10), and 0.05 (Fig. 11). In the figures, x' represents the coordinate along the surfaces of the baseplate and ribs. As for the smooth channel case, each local heat transfer coefficient was evaluated by averaging the values recorded, at corresponding positions, for the two adjacent symmetrical channels.

The local heat transfer data in all of the figures display a common behaviour. In general, heat transfer coefficients start from high values at the leading edge and then sharply decrease, reaching a very low value at the junction between the baseplate and the first rib. From this point on, the variations in heat transfer coefficients along the wall profile coordinate are periodic in nature and the periodicity is equal to the rib pitch (projected on the x'-coordinate). Two regions showing different thermal behaviour can be identified: the rib and the inter-rib regions. First, attention is focused on the thermal performance along the ribs. Heat transfer coefficient distributions along the horizontal surfaces of ribs indicate that the main flow tends to bypass the protruding elements, which act as obstacles to the induced convection currents. Conversely, effective heat transfer conditions occur along the vertical sides of ribs (especially at their leading edges) since they are washed by a relatively cool air flow. Along the inter-rib regions, heat transfer coefficient distributions are characterised by very low values close to the ribs, for the reason previously mentioned. However, the space between ribs is sufficient for the main flow to wash the inter-rib surfaces before being deflected by the next rib downstream. This explains the presence of the heat transfer coefficient peaks approximately at the midpoint of each inter-rib region. As previously noted, distributions of heat transfer coefficients between subsequent couples of ribs are similar; however, comparisons of h values at points separated by an elevation equal to the rib pitch exhibit a progressive reduction from the bottom to

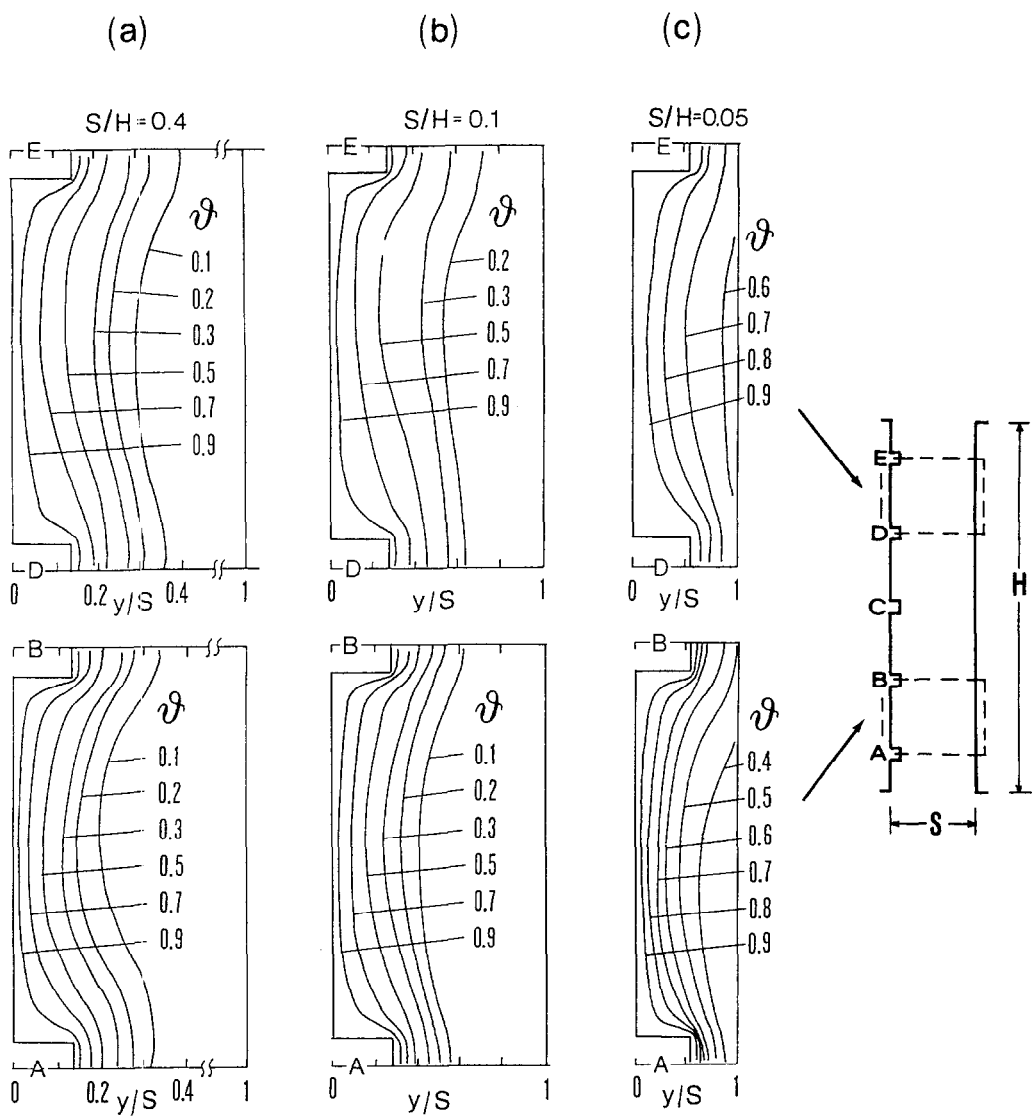

Fig. 8. Isotherm contours for the bottom and top modules, ribbed plate configuration, $Ra = 1.8 \cdot 10^7$; (a) $S/H = 0.4$, (b) $S/H = 0.1$, (c) $S/H = 0.05$.

the top of the channel. This is due to the developing thermal field and to the definition of heat transfer coefficient here assumed, h being based on the temperature difference between the heated wall and the inlet (not bulk) fluid.

The channel spacing slightly affects local heat transfer coefficients only along the vertical sides of first two ribs on passing from $S/H = 0.4$ (Fig. 9) to $S/H = 0.1$ (Fig. 10). As S/H is further reduced ($S/H = 0.05$, Fig. 11), the throughflow becomes very weak and is rapidly heated as approaches the channel exit section. As a consequence, h values at specified locations are clearly reduced, with the exception of the vertical side of the first rib, where the reduction in the cross-sectional area of the channel increases the local velocity of the flow.

Average heat transfer coefficients are shown in Fig. 12. The values h_{av} and h_o obtained by two different procedures are presented. Heat balance and optical results show the same trends and differ from each other by within 6%. The largest differences were recorded at the lowest S/H, where uncertainties related to the calculated radiation losses (affecting h_{av}) and in optical data (affecting h_o) are highest. It is apparent from the figure that even for the ribbed channel there is an optimum aspect ratio that maximises heat transfer (S/H about 0.1, to which corresponds $e/S = 0.28$). For larger aspect ratios (S/H up to 0.4), the average heat transfer coefficient is slightly lower (by about 5%) while, on passing from $S/H = 0.1$ to 0.05, the reduction is greater (about 25%).

Dimensionless heat transfer results for the ribbed channel are summarised in Fig. 13 and compared with those for the smooth channel. The presentation of data is performed on the basis of the channel Nusselt number against the channel Rayleigh number. The

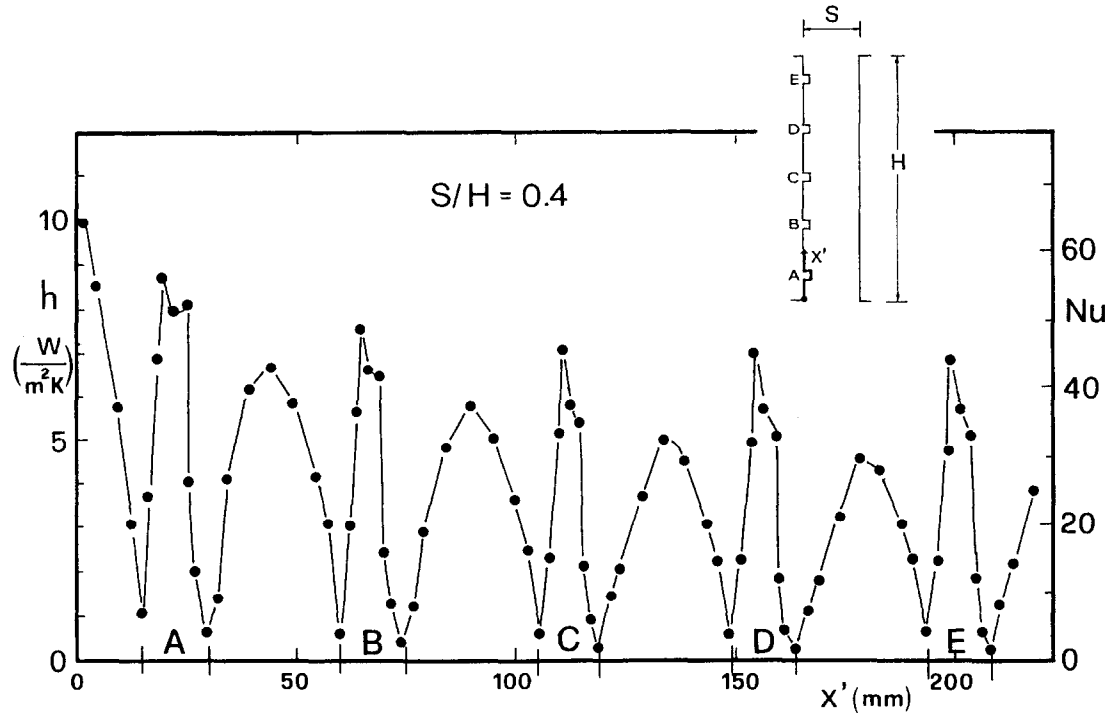

Fig. 9. Distribution of the heat transfer coefficient (and Nusselt number), ribbed plate configuration, $Ra = 1.8 \cdot 10^7$, $S/H = 0.4$.

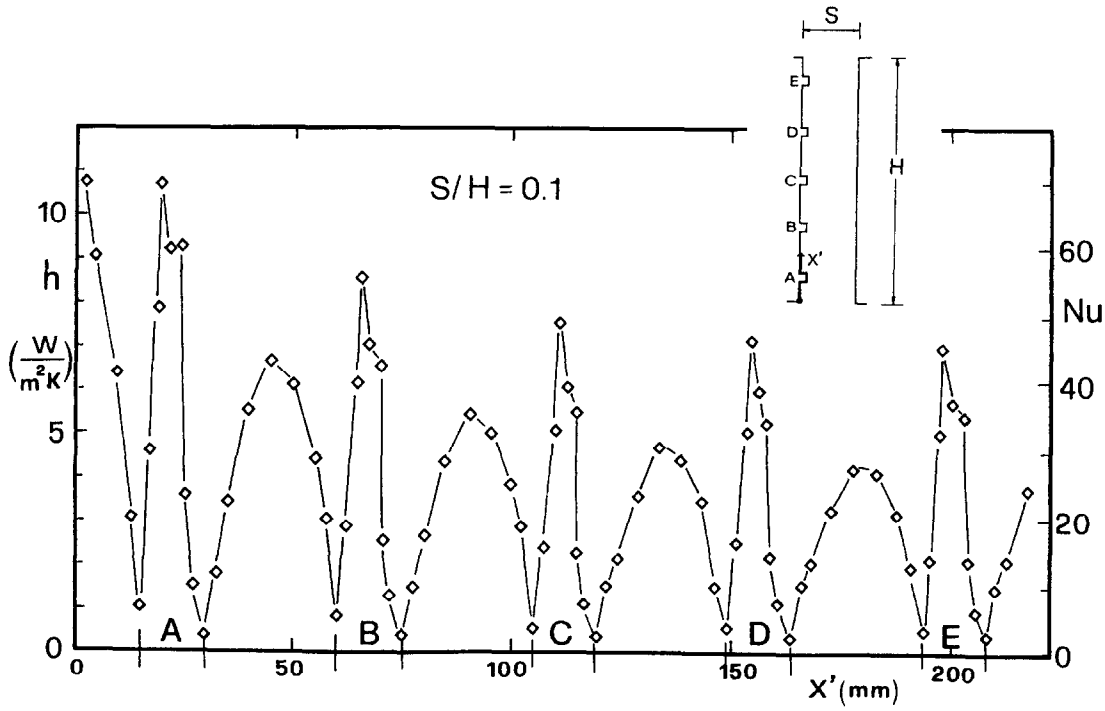

Fig. 10. Distribution of the heat transfer coefficient (and Nusselt number), ribbed plate configuration, $Ra = 1.8 \cdot 10^7$, $S/H = 0.1$.

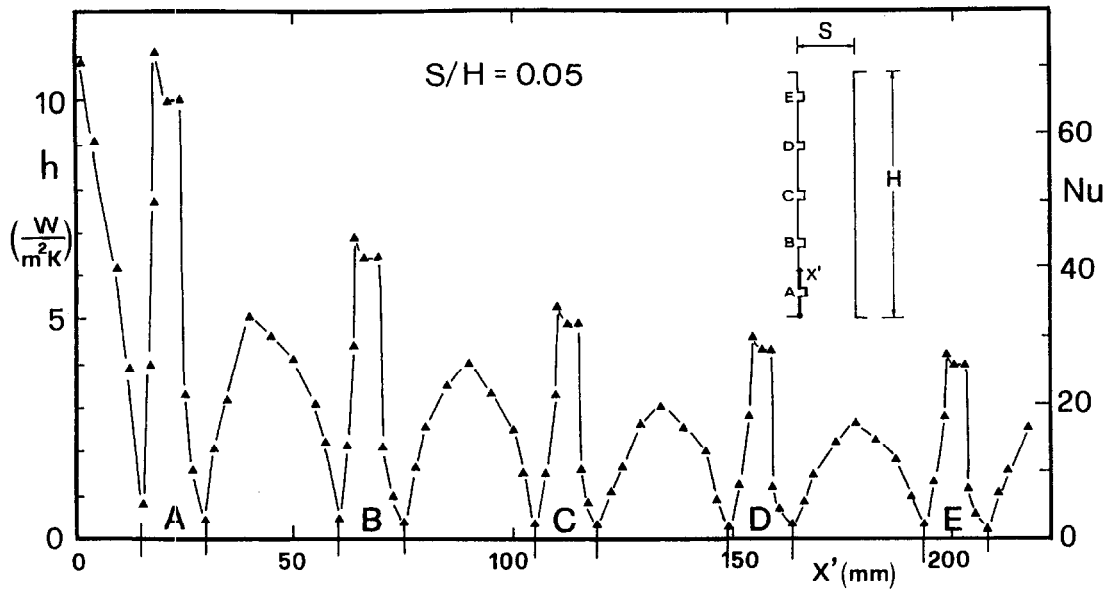

Fig. 11. Distribution of the heat transfer coefficient (and Nusselt number), ribbed plate configuration, $Ra = 1.8 \cdot 10^7$, $S/H = 0.05$.

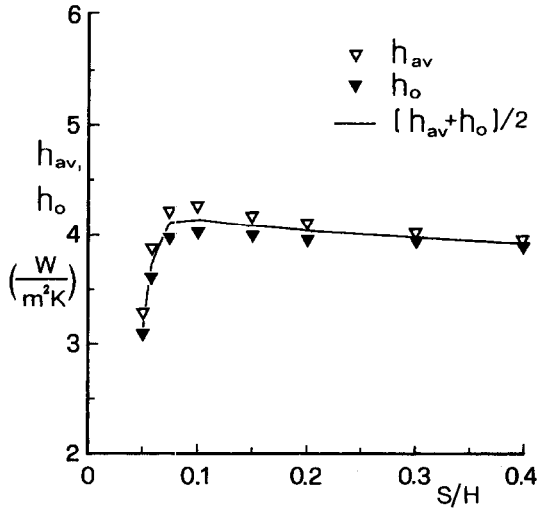

Fig. 12. Average heat transfer coefficients h_{av} (from the energy balance) and h_o (from integration of optical data), ribbed plate configuration ($Ra = 1.8 \cdot 10^7$).

ribbed channel results plotted on the graph were obtained for S/H ranging from 0.05 to 0.4 and for wall-to-fluid temperature differences from 10 to 45 K. In these ranges of parameters the buoyancy-induced flow was laminar. Ribbed channel results always fall below the line fitting the smooth channel results.

The majority of the rough channel data are well correlated by the relationship

$$Nu^* = 0.41(Ra^*)^{0.25}. \quad (14)$$

It should be noted that for the lowest S/H values (or for the highest e/S values) results do not fall on the same line. It means that the channel Rayleigh number alone does not properly express the effect of $(T_w - T_\infty)$ and geometric parameters, as occurs for the smooth channel case. This suggests that the Rayleigh number, S/H, and e/S (P/e being fixed) are likely to act as independent parameters. Therefore, the relationship (14) is valid in the following ranges of parameters:

$P/e = 7.2$;
$Ra^* \cong 2 \cdot 10^2 - 5 \cdot 10^5$;
$S/H \geqslant 0.075$
$e/S \leqslant 0.37$
$(T_w - T_\infty) \cong 10$–$45$ K.

Of particular interest is the comparison depicted in Fig. 14. Here the ratio between average Nusselt numbers pertaining to the ribbed and smooth plate $Nu_{av,r}/Nu_{av,s}$ is plotted as a function of the aspect ratio, the Rayleigh number being fixed ($Ra = 1.8 \cdot 10^7$). In addition, the ratio Q_r/Q_s (between the convective heat transfer rates from the ribbed and smooth plate) is reported. The ratio between convective heat transfer rates takes into account the increase in heat transfer surface area introduced by adding the ribs. As is evident from inspection of the figure, comparison in terms of average Nusselt numbers (i.e. heat transfer coefficients) shows 28% to 44% reductions due to the presence of ribs. On the basis of convective heat transfer rates, the comparison is not so unfavourable (reductions between 8% and 28%): however, the increase in heat transfer surface area due to the ribs does not compensate for the decrease in heat transfer coefficient. The results presented here are in good agreement with the findings of Bhavnani and Bergles [5], who recorded a 23% reduction in heat transfer

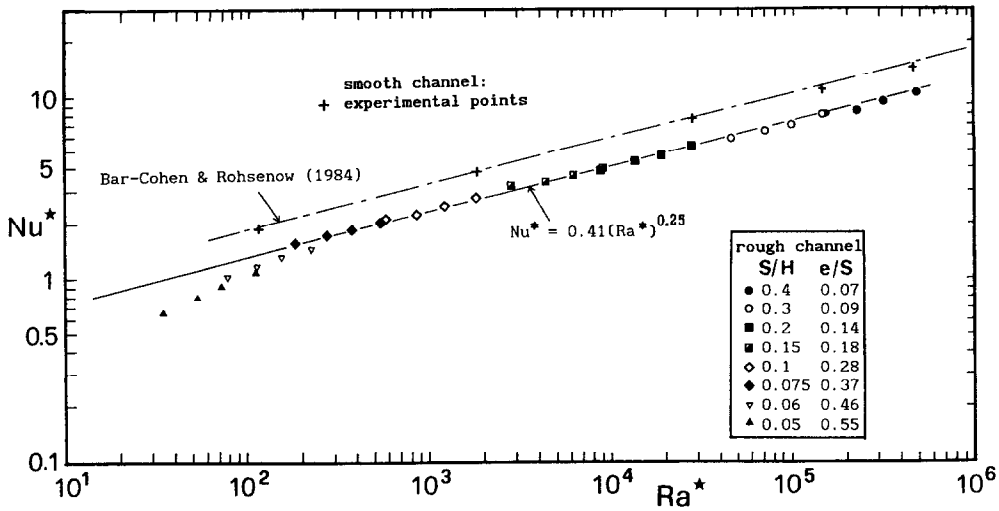

Fig. 13. Channel Nusselt number against the channel Rayleigh number.

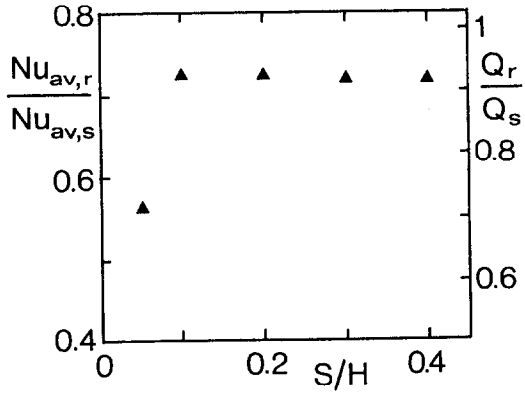

Fig. 14. Average Nusselt numbers and heat transfer rules of the ribbed plate, normalised by the values for the smooth plate.

coefficient and a 10% reduction in heat transfer rate when roughening by square ribs (at $P/e = 8$) a vertical isothermal surface. What the present study points out is the further reduction associated with the narrowest channels.

The quantitative assessment of heat transfer reductions due to the ribs is particularly important in the field of electronic equipment, whose thermal design is often based on smooth plate correlations; neglecting the effect of the protrusions constituted by the microelectronic chips could lead to underestimation of the working temperature of the components, especially in the case of narrow channels.

CONCLUSIONS

Natural convection heat transfer was experimentally investigated for vertical channels formed by a heated ribbed surface and an opposing unheated smooth surface. The effects of the channel spacing and the Rayleigh number were studied, while the geometry and the pitch of the transverse ribs were kept fixed. A systematic database for heat transfer characteristics in such geometric and thermal conditions was established. For the purpose of comparison, additional experiments were performed for vertical channels without ribs. A schlieren optical technique was used to reconstruct the distribution of temperature in the convective flow and to obtain local heat transfer coefficients.

In the ribbed channel, protrusions tend to inhibit heat transfer from the surface regions just upstream and downstream of the ribs. Effective heat transfer conditions are recovered approximately at the midpoint of the inter-rib region and along the vertical sides of ribs. Comparison of the average heat transfer coefficients and overall heat transfer rates for the ribbed channel with those for the smooth channel shows decreased heat transfer performance for the ribbed channel.

Flow resistances due to the obstructions have a larger impact on heat transfer for the narrowest ribbed channel studied ($S/H = 0.05$, corresponding to $e/S = 0.55$). In this condition, reductions in heat transfer, as compared with the smooth channel configuration, are even higher.

In conclusion, the experiments reported here indicate that adding ribs to a smooth plate for the purpose of heat transfer augmentation (as successfully occurs in forced convection) is useless, in the ranges of parameters studied, for natural convection. In applications where large-scale roughness occurs naturally, the thermal design must take into account the role played by the roughness elements, especially if they are fitted in narrow passages.

REFERENCES

1. A. Bar-Cohen and W. M. Rohsenow, Thermally optimum spacing of vertical, natural convection cooled, parallel plates, *ASME J. Heat Transfer*, **106**, 116–123 (1984).
2. Y. H. Hung and W. M. Shiau, Local steady-state natural

convection heat transfer in vertical parallel plates with a two-dimensional rectangular rib, *Int. J. Heat Mass Transfer*, **31,** 1279–1288 (1988).
3. S. A. M. Said and R. J. Krane, An analytical and experimental investigation of natural convection heat transfer in vertical channels with a single obstruction, *Int. J. Heat Mass Transfer*, **33,** pp. 1121–1134 (1990).
4. Y. Joshi, T. Willson, and S. J. Hazard, III, An experimental study of natural convection from an array of heated protrusions on a vertical surface in water, *ASME J Electronic Packaging*, **111,** 121–128 (1989).
5. S. H. Bhavnani and A. E. Bergles, Effect of surface geometry and orientation on laminar natural convection heat transfer from a vertical flat plate with transverse roughness elements, *Int. J. Heat Mass Transfer*, **33,** 965–981 (1990).
6. K. M. Kelkar, and D. Choudhury, Numerical prediction of periodically fully developed natural convection in a vertical channel with surface mounted heat generating blocks, *Int. J. Heat Mass Transfer*, **36,** 1133–1145 (1993).
7. S. Acharya and A. Mehrotra, Natural convection heat transfer in smooth and ribbed vertical channels, *Int. J. Heat Mass Transfer*, **36,** 236–241(1993).
8. G. Tanda, Natural convection heat transfer from a staggered vertical plate array, *ASME Journal of Heat Transfer*, **115,** 938–945 (1993).
9. F. Devia, G. Milano, and G. Tanda, Evaluation of thermal field in buoyancy-induced flows by a schlieren method, *Experimental Thermal and Fluid Science*, **8,** 1–9 (1994).
10. G. Tanda, Application of optical methods to the study of convective heat transfer in rib-roughened channels, Ph.D.Thesis, Department of Mechanical Engineering and Aeronautics, City University, London (1996).
11. R. J. Moffat, Describing the uncertainties in experimental results, *Experimental Thermal and Fluid Science*, **1,** 3–17 (1988).